

On the X-ray haloes of the Galaxy and the Local Group and the diffuse soft X-ray background

S.D. Sidher^{1,2}, T.J. Sumner¹, and J.J. Quenby¹

¹ Astrophysics Group, Blackett Laboratory, Imperial College of Science, Technology and Medicine, London SW7 2BZ, England, UK

² Space Science Department, Rutherford Appleton Laboratory, Chilton, Didcot, Oxfordshire OX11 0QX, England, UK

Received 15 January 1998 / Accepted 10 December 1998

Abstract. We have extended the spectral modelling of the soft X-ray background (SXR) using the ROSAT PSPC data along several lines of galactic longitude. Our results continue to demonstrate the need for a Galactic halo component, which is shown to vary markedly as a function of position. These fluctuations significantly affect the ability to investigate variations in the extragalactic SXR below 2 keV. Our conclusions do not support the proposal of an X-ray halo surrounding the Local Group of galaxies as invoked by Suto et al. (1996).

Application of the 3 component model to a deep ROSAT observation in the direction of the Lockman hole is also discussed.

Key words: X-rays: ISM – ISM: structure – ISM: individual objects: Draco complex – ISM: clouds – ISM: general

1. Introduction

Recent interest in the properties of the Galactic halo arises from two important considerations. Firstly, the observations of galactic gas motions, energetic radio emission from other spiral galaxies and cosmic ray-interstellar gas interactions all appear to support a dynamic halo model, generically known as the fountain model (Shapiro & Field 1976, Kahn 1994). It has been suggested that cosmic rays may drive the vertically upward flow far out (Breitschwerdt et al. 1993). However, according to Bloemen et al. (1993), electron radiation from an edge-on spiral galaxy suggests that energetic electron acceleration and energy loss occurs close to the local disk regions, and not in the thick extended halo. The implication is that structures seen down to the resolution of 350 pc may extend far above the disk. Hence a patchy Galactic halo is plausible.

Secondly, the effect of any halo fluctuations on the diffuse soft X-ray background (SXR) correlation function may be significant, with the additional possibility of it having an impact on the microwave anisotropy. Hot intracluster gas is an important baryonic component and may contribute up to 30% of the total gravitational mass of rich clusters (White et al. 1993). Suto et al. (1996) have suggested that a halo to our Local Group

(LG) could contribute significantly to 1 keV background and also produce a measurable component of the microwave background quadrupole anisotropy. However, Pildis & McLaugh (1996) find data from other poor groups which do not support this hypothesis.

The importance of low energy X-ray data in determining background mass has been highlighted by the detection of excess EUVE emission from the Coma cluster direction (Lieu et al. 1996). The authors suggest that $\sim 10\%$ of the gravitational mass is in the form of rapidly cooled $\sim 8 \cdot 10^5$ K gas. This observation is dependent on correctly establishing the Galactic background and absorption effects.

In this paper we report on detailed spectral modelling which has been undertaken to better establish the mean and fluctuating components of the Local Hot Bubble (LHB), embedded disk and halo contributions to the SXR. The data employed are from the ROSAT PSPC observations taken along lines of fixed galactic longitude. A deep observations in the Lockman hole region is also considered. The implication of our results on the galactic structure and on the cosmology-related problems is discussed.

2. Spectral model

The spectral modelling is done using a series of “slabs” which are set up to represent hot gas emission regions and cold gas absorbing layers (Sidher et al. 1996, see also Pietz et al. 1998 and references therein for similar analyses). In this work the furthestmost slab defines the extragalactic component of the SXR, which is taken to have a power law source spectrum of spectral index 1.4. The next two slabs contain a hot gas component, which we associate with the Galactic halo, and the cold absorbing Galactic disk (see Sidher et al. 1996 for justification of this). The closest slab to us then contains the hot gas component within the local cavity plus a small amount of intermixed absorbing material. The radiation transfer function through each slab is

$$I_f(E) = I_i(E)e^{-n_H\sigma(E)l} + \frac{n_e^2 P(E, T)}{n_H\sigma(E)} \left(1 - e^{-n_H\sigma(E)l}\right) \quad (1)$$

where $I_i(E)$ is the incident radiation entering the shell from the outside, E is the photon energy, $\sigma(E)$ is the energy dependant

absorption cross-section, n_e is the electron density, n_H is the HI column density, T is the temperature and l is the depth of the shell. $P(E, T)$ is the radiative power loss function for a plasma at a temperature T . In this work the Landini & Monsignori Fossi plasma code has been used to model the emission from the hot gas components in the halo and the local cavity (Landini & Monsignori Fossi 1990). The HI absorption column in the cold gas of the disk has been derived for each pointing direction using the Stark catalogue (Stark et al. 1992; For a comparison with the more recent Leiden/Dwingeloo 21-cm line survey (Hartmann & Burton 1997) see the discussion in Sect. 3.1). The absorption cross-section as a function of energy is taken from Morrison & McCammon (1983). To economise on computing time the local cavity hot gas temperature is kept fixed at $\log T = 5.9$ with an intermixed column density of $6.6 \cdot 10^{18} \text{ cm}^{-2}$ (see Juda et al. 1991 and Lieu et al. 1992). During the fitting procedure the emission measure (EM) for both the local cavity and the halo component are treated as free variables. In addition the temperature of the halo component is allowed to vary. For each combination of parameters the spectrum arriving at the telescope aperture is modelled with a 1 eV resolution between 50 eV and 3 keV. This modelled spectrum is then convolved with the ROSAT PSPC energy response function and the predicted spectrum is binned at 50 eV intervals. The predicted binned spectrum is then compared with the observed spectrum over the entire PSPC energy range using standard χ^2_ν .

3. Data analysis

PSPC spectral data were extracted from a region of radius 0.2° and binned at 50 eV intervals. Procedures recommended by Plucinsky et al. (1993) for accepting valid event data were followed. Care was taken to ensure that the region selected was free from all obvious X-ray sources. The extracted data were then further corrected for the effects of vignetting, exposure and detector dead time.

3.1. Galactic latitude survey for different lines of galactic longitude

We extracted as many available ROSAT PSPC observations from the archive as possible, ensuring a fairly uniform sampling interval in galactic latitude for longitudes 40° , 60° , 90° , 120° and 145° . The slab model was then applied to each observation using the appropriate HI column density for each region. Values for the three free parameters (viz. foreground EM, halo temperature and EM) were obtained from the best spectral fits. The complete results of this investigation are presented in Table 1. The best fit halo temperature is not included in this table as it was found to lie in the rather narrow range of $\log T = 6.3 \pm 0.1$ for all directions. In general the low galactic latitude regions in our sample provided the poorer fits to the model and are therefore excluded from the table. This is not a surprising result as the observer's line of sight passes through more of the complex Galactic disk structure with decreasing latitude. Satisfactory spectral fits were however obtained for the majority of observations at $|b| \geq 35^\circ$.

Table 1. Results of fitting three component models to PSPC observations of all galactic longitude strips. The last entry is for the deep observation in the Lockman hole region.

Gal Long	Gal Lat	Halo Emission Measure	Foreground Emission Measure	χ^2_ν
l [$^\circ$]	b [$^\circ$]	$\times 0.0032$ ($\text{cm}^{-6} \text{ pc}$)	$\times 0.0032$ ($\text{cm}^{-6} \text{ pc}$)	
43.52	+85	1.72±0.28	1.75±0.13	1.7
35.42	+79	4.06±0.41	3.81±0.19	1.2
35.63	+78	2.34±0.34	1.72±0.13	2.9
36.87	+68	4.54±0.69	1.16±0.19	1.8
41.88	+53	7.56±2.41	1.34±0.19	1.6
43.84	+49	12.63±0.69	1.00±0.10	3.9
35.30	+45	4.53±0.45	1.13±0.06	2.9
35.33	+36	23.19±1.00	2.81±0.09	3.0
36.31	-36	12.09±0.41	1.44±0.03	3.8
38.93	-47	5.84±0.59	0.94±0.09	1.5
40.64	-48	5.53±0.50	1.23±0.06	2.1
36.50	-51	10.31±0.75	1.69±0.16	2.2
39.76	-52	7.56±0.59	1.84±0.13	1.8
36.14	-56	4.97±0.25	1.03±0.06	1.3
35.89	-79	3.50±0.53	1.34±0.13	0.9
38.10	-62	4.15±0.34	1.25±0.06	2.9
63.95	-88.2	8.05±0.05	0.18±0.07	4.3
64.08	-58.8	5.20±0.30	1.04±0.04	3.7
61.15	-52.2	11.0±4.00	1.40±0.20	1.0
58.96	-48.8	7.70±0.20	0.79±0.04	3.8
56.26	-42.5	8.85±1.25	1.14±0.09	0.9
59.71	-39.1	7.00±0.15	1.52±0.06	1.6
60.77	-35.5	11.5±0.50	1.34±0.06	1.4
58.15	+37.5	5.20±0.40	1.30±0.10	3.4
63.60	+38.9	9.70±0.60	2.00±0.15	3.5
57.82	+55.9	5.00±1.00	0.85±0.25	1.6
63.16	+58.3	2.65±0.15	0.95±0.10	3.0
61.45	+83.1	4.70±0.30	1.26±0.04	2.5
85.52	-85	3.94±0.41	1.22±0.10	1.8
91.93	-76	2.95±0.45	1.41±0.19	2.2
92.47	-67	6.6±2.8	1.41±0.31	0.7
88.52	-60	5.1±0.4	1.38±0.06	2.2
88.27	-55	8.25±2.25	1.13±0.19	1.7
90.45	-44	3.3±0.4	0.88±0.06	1.5
86.11	-38	12.2±4.2	1.47±0.16	1.0
90.07	-34	8.25±2.25	1.41±0.09	2.1
87.60	+35	10.1±0.6	0.97±0.06	4.3
89.52	+39	7.25±0.77	1.38±0.16	1.3
92.58	+40	6.0±0.4	2.38±0.16	2.0
91.49	+47	4.75±0.5	3.44±0.19	1.1
87.01	+60	4.55±0.25	2.84±0.09	2.6
89.03	+63	8.6±2.1	2.72±0.59	1.4
85.52	+67	5.0±1.2	2.69±0.16	2.5
88.63	+72	4.9±0.6	2.22±0.19	3.2
87.40	+74	7.35±0.45	2.94±0.19	1.7
86.36	+75	7.7±0.4	2.38±0.16	3.0
85.72	+83	4.2±0.4	1.22±0.12	3.5
122.2	+61.0	3.22±1.22	1.66±0.34	1.0
123.5	+54.0	2.94±0.31	1.31±0.16	1.0
117.6	+51.0	2.88±0.06	2.00±0.06	2.7
119.1	+48.0	5.72±1.09	1.41±0.41	0.6

Table 1. (continued)

Gal Long	Gal Lat	Halo Emission Measure $\times 0.0032$ (cm^{-6} pc)	Foreground Emission Measure $\times 0.0032$ (cm^{-6} pc)	χ^2_ν
ℓ [$^\circ$]	b [$^\circ$]			
115.0	+47.0	2.94±0.12	1.53±0.06	1.5
121.5	+45.0	8.41±2.25	2.97±0.53	1.8
123.6	+41.0	10.88±4.03	0.97±0.16	0.7
124.6	-32.0	19.25±3.03	1.00±0.10	2.2
118.6	-38.0	10.12±2.03	1.31±0.31	1.5
123.8	-50.0	7.09±3.06	1.00±0.20	0.7
117.9	-56.0	7.09±1.00	0.81±0.20	0.8
120.2	-62.0	6.06±2.03	1.41±0.20	1.6
122.3	-72.0	7.09±2.03	0.81±0.10	2.6
140.5	+86.2	2.62±0.35	1.46±0.15	3.3
140.2	+78.9	2.00±0.35	2.38±0.14	2.8
145.6	+65.0	2.94±0.09	1.02±0.04	1.4
142.2	+59.4	2.14±0.16	1.74±0.08	2.8
142.5	+54.5	1.56±0.32	1.28±0.13	1.3
143.6	+48.6	1.19±0.19	1.75±0.05	2.0
145.7	+43.1	12.70±0.95	1.45±0.06	1.2
141.2	+38.9	4.16±0.06	1.34±0.08	1.6
144.6	-36.2	41.50±2.84	1.65±0.11	1.9
148.5	-43.8	42.23±2.40	1.32±0.04	4.5
141.6	-47.4	39.09±2.03	4.90±0.16	1.7
144.0	-54.6	7.10±0.33	1.14±0.08	1.9
147.0	-59.1	2.82±0.52	0.88±0.08	4.9
145.5	-65.9	6.78±0.05	0.86±0.07	3.8
149.5	-84.2	3.07±0.24	1.12±0.05	2.9
149.5	+53.2	1.50±0.50	1.00±0.40	5.1

The results for all the regions are summarised in Figs. 1 to 3 using the Hammer-Aitoff projection of the sky in galactic coordinates. The fitted halo EM for each direction is shown as an open circle. The diameter of each circle is proportional to the halo emission component at that point. The labelled contours represent the expected EM variation if the hot gas is associated with the spiral arms and calculated from the following expression (see Sidher et al. 1996)

$$EM = A^2 \int_{z_0/\sin b}^{\infty} \left[\frac{e^{-l \sin b/h}}{r_l^p} \right]^2 dl \quad (2)$$

where A is a factor associated with the local halo density in the solar neighbourhood, z_0 is the disk height above the galactic plane marking the start of the halo, b is the galactic latitude, h is the scale height above the plane of the disk, l is the distance along the line of sight, p determines the radial halo mass distribution in the Galaxy and r_l is the radial distance from the Galactic centre given by

$$r_l = \sqrt{l^2 \cos^2 b + R_0^2 - 2lR_0 \cos b \cos \ell} \quad (3)$$

R_0 , the distance of the Sun from the Galactic centre, is taken to be 8 kpc. The halo emission contours in Fig. 1 show no longitude structure; the reason for this is apparent from Eq. 1 as the term

in the denominator becomes unity for no radial dependence ($p=0$). Figs. 2 and 3 show the same set of fitted halo emission measures, except that the contours now denote a radial mass distribution following dark matter ($p=2$) and luminous matter ($p=3$) respectively. In all three cases a disk thickness of 3 kpc and a halo scale height of 12 kpc are assumed following the model proposed by Bloemen (1987) for stability at $\log T = 6.3$. The maximum halo path-length, or the halo cut-off, is set at 50 kpc and the electron density is fixed at 0.0025 cm^{-3} .

Fig. 4 shows the best fit χ^2_ν values for the fitted halo emission measures as plotted in each of the previous three figures. In general there appears to be no significant pattern between the map of Fig. 4 and any of the maps of Figs. 1, 2 and 3, for example the high χ^2_ν points do not belong to a group with high emission components.

The mean value of our fitted halo emission measures (excluding the three very high values) is $0.020 \text{ cm}^{-6} \text{ pc}$. The standard deviation (see Fig. 5) is 60% of this value (again excluding the three very high values) at $0.012 \text{ cm}^{-6} \text{ pc}$. Although our halo emission measures compare favourably with the range $\sim 0-0.017 \text{ cm}^{-6} \text{ pc}$ derived by Snowden et al. (1998) from their detailed analysis of $\frac{1}{4}$ keV band data, the foreground emission measures in our sample do not support their conclusion that the bulk of the SXR originates inside the LHB. Our results are in broader agreement with those of Pietz et al. (1998).

To check how much of the EM variation might be due to small-scale variability in the column density which would not be picked up by the Stark catalogue, column densities have also been recovered from the Leiden/Dwingeloo survey (Hartmann & Burton 1997). The Stark and Leiden/Dwingeloo column densities for all our pointing directions are compared in Fig. 6. As well as a random scatter of a few 10^{20} cm^{-2} there is a small systematic difference. To estimate the effect of this on the derived Galactic halo EM it is necessary to consider the effect on absorption in the 400–500 eV energy range where the halo has its most dominant effect on the spectrum (see Fig. 7). From Morrison & McCammon (1983) the absorption cross section in this region is $\sim 7.4 \cdot 10^{-22} \text{ cm}^{-2}$. The solid line in Fig. 8 shows how the difference in column density between the Leiden/Dwingeloo survey values and the Stark values would affect the halo EM. The symbols on the figure show the difference between the actual fitted value and the mean. The scatter shown in the plot is far in excess of that expected on the basis of column density uncertainties, from which we conclude that the scatter reflects a real intrinsic variation in the halo EM. The fact that the Leiden/Dwingeloo column density values are about 8% lower than from Stark has a negligible effect on our results.

An additional source of Galactic and nearby halo absorption, not taken into account in the modelling of Sect. 2, is the warm, diffuse H^+ component of the ISM. This gas, believed to be at $\sim 10^4 \text{ K}$, constitutes a quarter of the interstellar hydrogen. It extends out into the halo region with a scale height of about 900 pc. Detailed measurements of the latitude and longitude distribution are not available for H^+ , but we can use some figures supplied by Reynolds (1991) to estimate the additional error in our determination of the halo EM variability likely to arise from

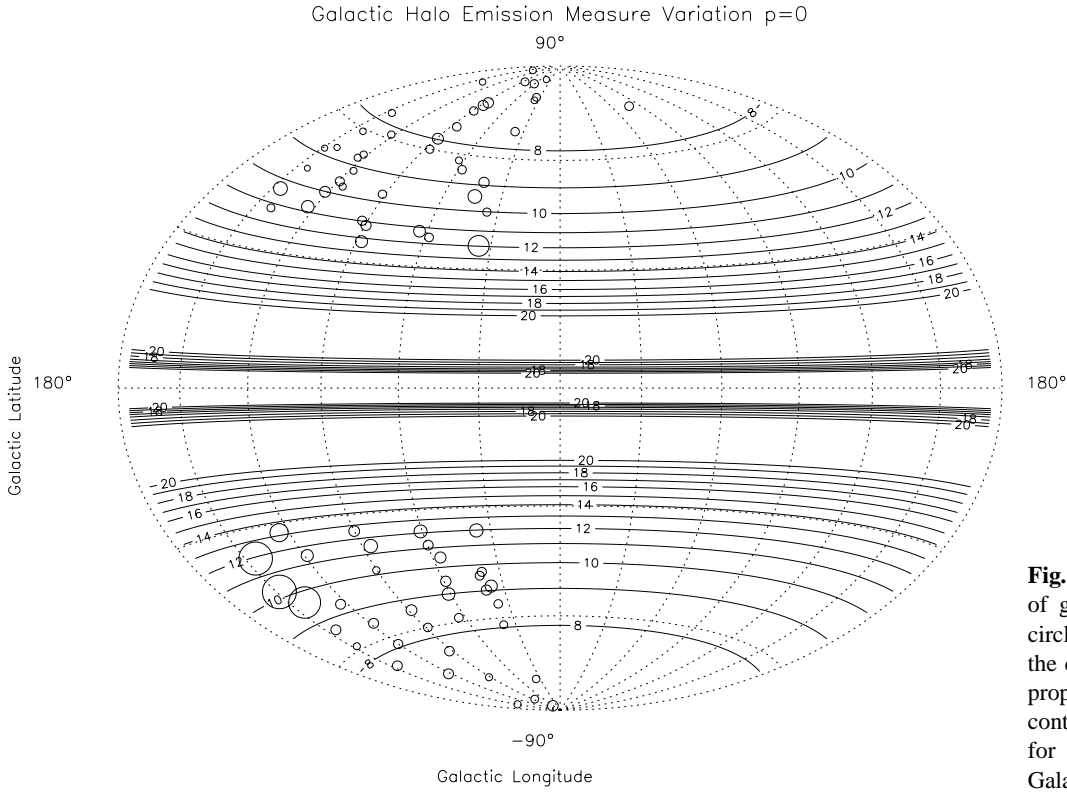


Fig. 1. Halo EM plotted as a function of galactic coordinates. The open circles represent the fitted halo EM, the diameter of each symbol being proportional to the emission. The contours represent the EM variation for a hot gas associated with the Galactic spiral arms ($p=0$).

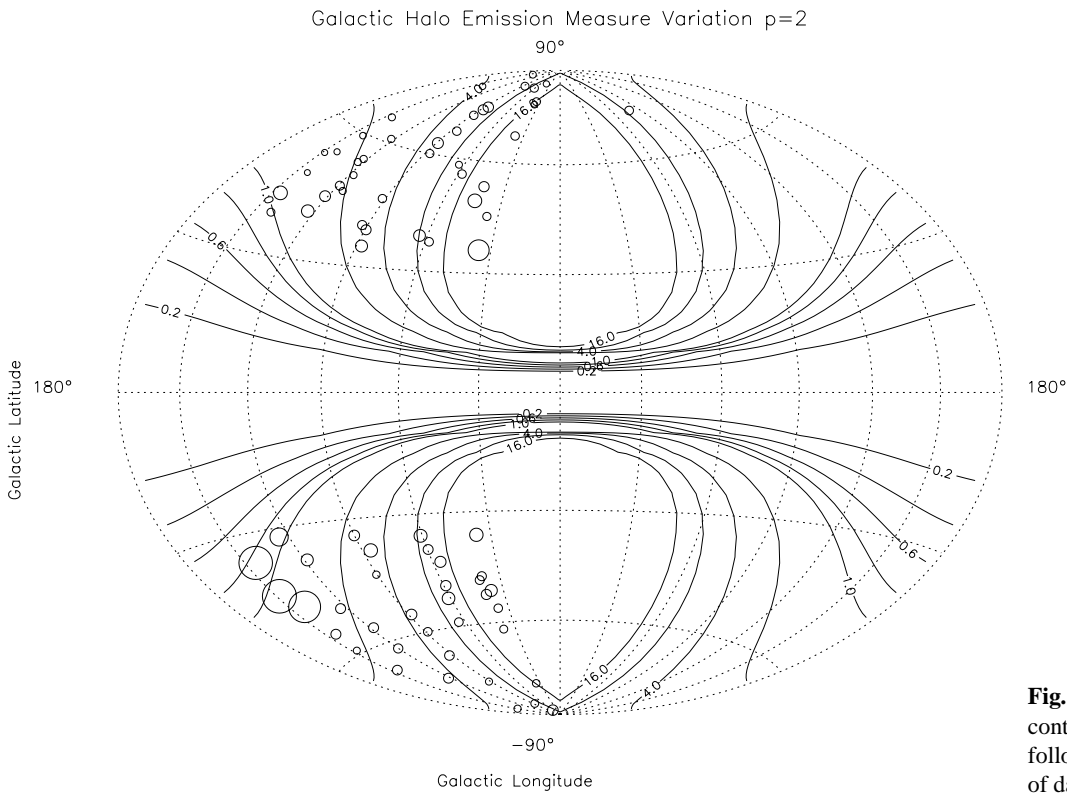


Fig. 2. Same as Fig. 1 but here the contours represent the EM variation following a radial mass distribution of dark matter ($p=2$).

this lack of knowledge. From Table 1 of Reynolds (1991) we notice that the H^+ column is both less than the HI column and less variable than the neutral hydrogen. However, there seems

to be some correlation of the variability. While N_{H^+} values range from $0.74 \cdot 10^{20} \text{ cm}^{-2}$ to $2.1 \cdot 10^{20} \text{ cm}^{-2}$, N_{HI} values range from $1.5 \cdot 10^{20} \text{ cm}^{-2}$ to $6.2 \cdot 10^{20} \text{ cm}^{-2}$. Now the peak

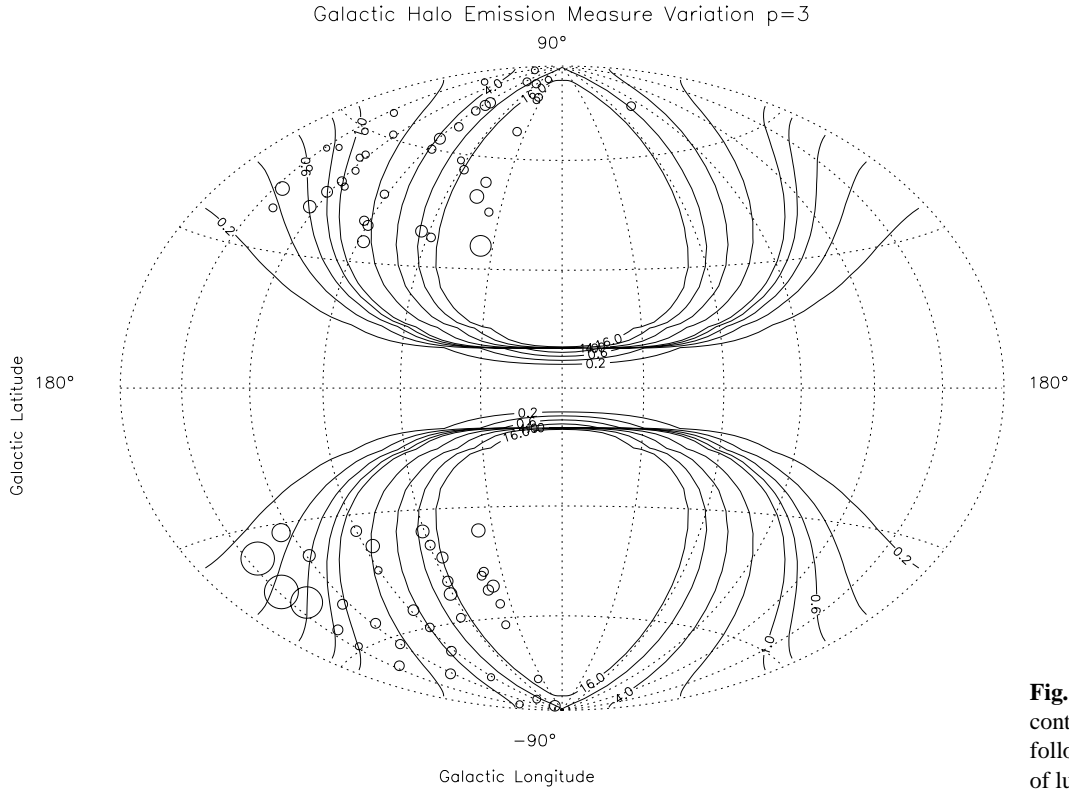


Fig. 3. Same as Fig. 1 but here the contours represent the EM variation following a radial mass distribution of luminous matter ($p=3$).

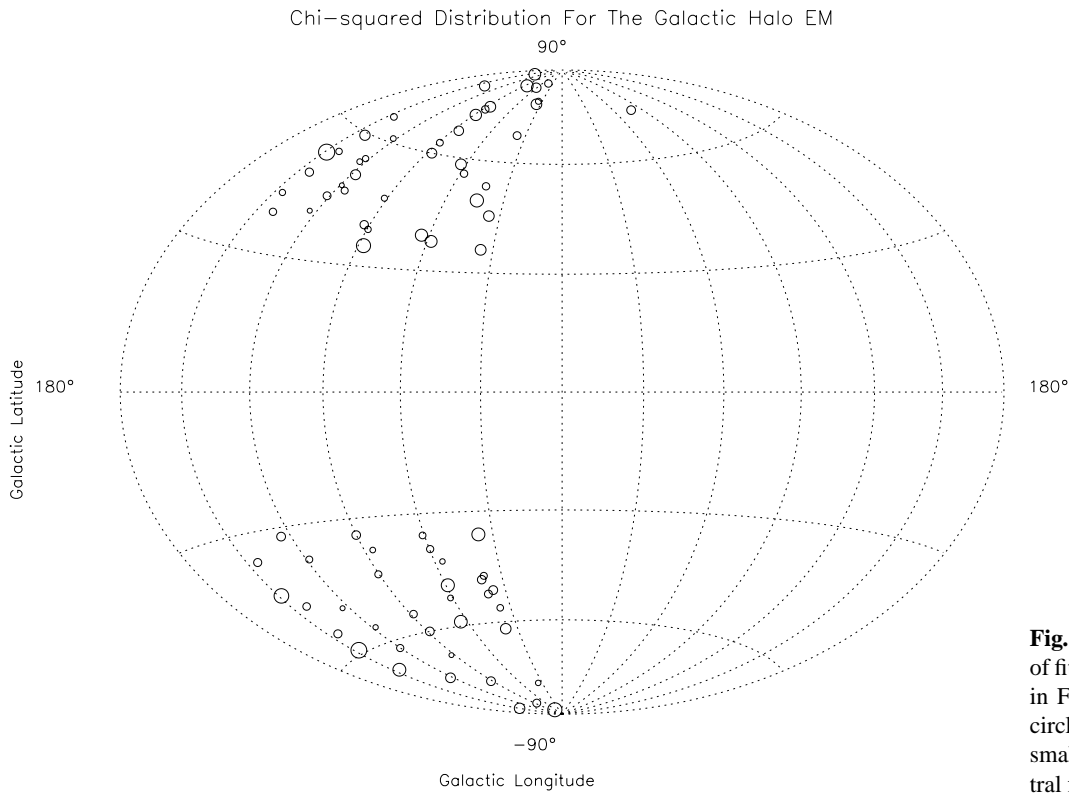


Fig. 4. Variation of χ^2_ν , the goodness of fit parameter for the regions fitted in Figs. 1–3. The diameter of each circle is proportional to χ^2_ν , i.e. the smaller the circle the better the spectral fit.

contribution to the counting rate (Fig. 7) from the halo occurs at about 200 eV. At this energy we assume that the absorption cross section per H^+ within an H II region of an O star is a reasonable

approximation to the H^+ cross section in a warm ISM gas. From Cruddace et al. (1974) we take this cross section to be $5 \cdot 10^{-21} \text{ cm}^{-2}$. For cold gas we estimate the HI cross section

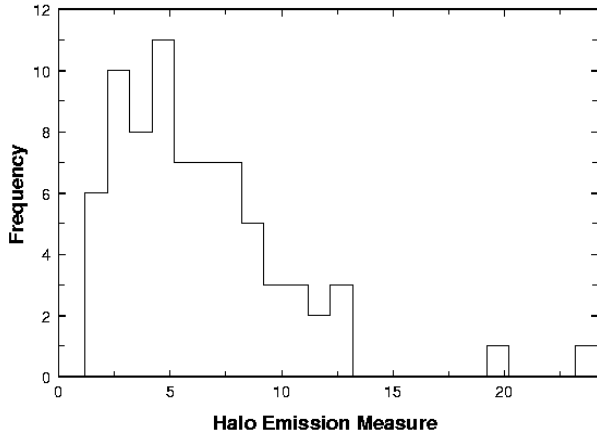


Fig. 5. Frequency distribution of the fitted halo emission measures (in units of $0.0032 \text{ cm}^{-6} \text{ pc}$) as given in Table 1.

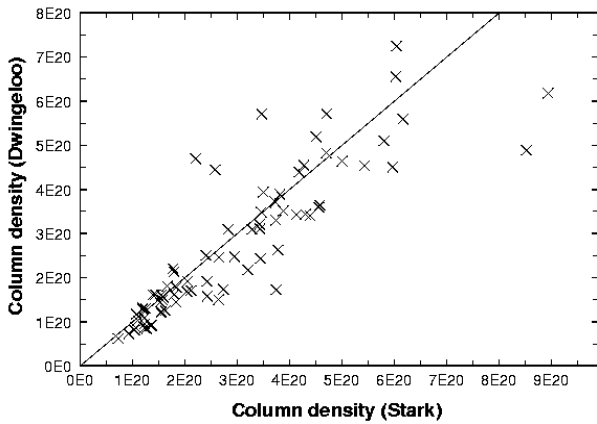


Fig. 6. Scatter plot of the Leiden/Dwingeloo HI survey data vs. the data from the Stark HI survey for all the directions in our sample.

to be $9 \cdot 10^{-21} \text{ cm}^{-2}$ (Morrison & McCammon 1983). We find a range of attenuations between 0.7 and 0.35 for the H^+ column and between 0.2 and 0.004 for the HI column, based on the Reynolds data. Thus the HI column variability dominates that of the warm gas and the latter is likely at the most to contribute a factor of two to the halo EM variability. In view of the fact that we find a halo emission varying by a factor 10 or more and also since we find this variability to be uncorrelated with likely errors in the cold gas column, we conclude it to be unlikely that the additional warm gas absorption can significantly affect our conclusions.

Fig. 7, which shows a typical fitted spectrum for a SXRb direction, clearly demonstrates that at 1 keV the halo component is about 10% of the extragalactic power law component. This suggests that at 1 keV the SXRb fluctuations can only be studied at the 10% level. Likewise, at 2 keV, it appears that fluctuations at just the 1% level can be examined.

3.2. Possibility of a Local Group halo

It can be argued that the component of emission attributed to the Galactic halo is in fact related to the hot gas associated with

the LG of galaxies (see Suto et al. 1996). To investigate this possibility we took the coordinates of the Andromeda nebula as being representative of the origin of the coordinate system for the LG. Doing the necessary coordinate transformations for all the regions in our sample we show in Fig. 9 the Hammer-Aitoff projection map in “Local Group” coordinates, with the fitted halo component now being associated with the LG. The contours represent the expected fall-off in the EM from the centre of the group assuming a simple $1/r^2$ (i.e. $p=2$) spherically-symmetric halo mass distribution. The actual expression used for EM variation as a function of LG coordinates is similar to Eq. 2 but without the term in the numerator for the disk dependence. For consistency with Suto et al. (1996) the distance from the LG centre to our Galaxy is maintained at 350 kpc.

There is no striking pattern apparent here and it is difficult to argue in favour of the conclusions drawn by Suto et al. (1996). It is unlikely that the emission originates from the LG, principally because of the large variations observed in the halo emission. For all the analyzed directions the data were arranged in the LG longitude bands of 30° width. The best fit value for the electron density is estimated to be $0.0004 \pm 0.0003 \text{ cm}^{-3}$. This value is an order of magnitude smaller than the one corresponding to the Galactic halo.

4. The Lockman hole

ROSAT PSPC datasets for the Lockman hole region (Lockman et al. 1986) were accessed from the archive with the criterion that they lie within or at the periphery of this lowest column density region. The common feature of these observations is that they are some of the deepest observations performed with ROSAT, thus providing an opportunity to improve upon the quality of the spectral fits than hitherto achieved.

These deep observations, however, initially gave quite poor fits to the data using the previously defined recipes. To investigate this effect further the time series for the total event count rate (TEVS) were examined for the Lockman hole observation centred at $\ell=149^\circ 5$, $b=53^\circ 2$ (ROSAT observation sequence number rp900029), which has a total exposure time of 122,123 seconds. The entire observation consists essentially of three viewing periods. Upon applying an additional constraint of a maximum total event rate of 14 cts s^{-1} the fluctuations in the time series become essentially insignificant, giving us confidence that most of the contaminating events have been removed from the data. The resultant exposure time for the observation was however reduced to just 9,278 seconds, typical of the exposures for the other PSPC fields listed in Table 1. The output spectra resulting from the good time windows used in generating these time series are plotted in Fig. 10. It is evident from the essential differences in the two spectra that the bump-like feature present at 550 eV, before application of the maximum total event rate cutoff, is a contaminant most likely to be associated with particle background enhancements. As the observation under consideration here commenced in April 1991 and completed in April 1992, the enhancements could therefore be connected with the solar maximum.

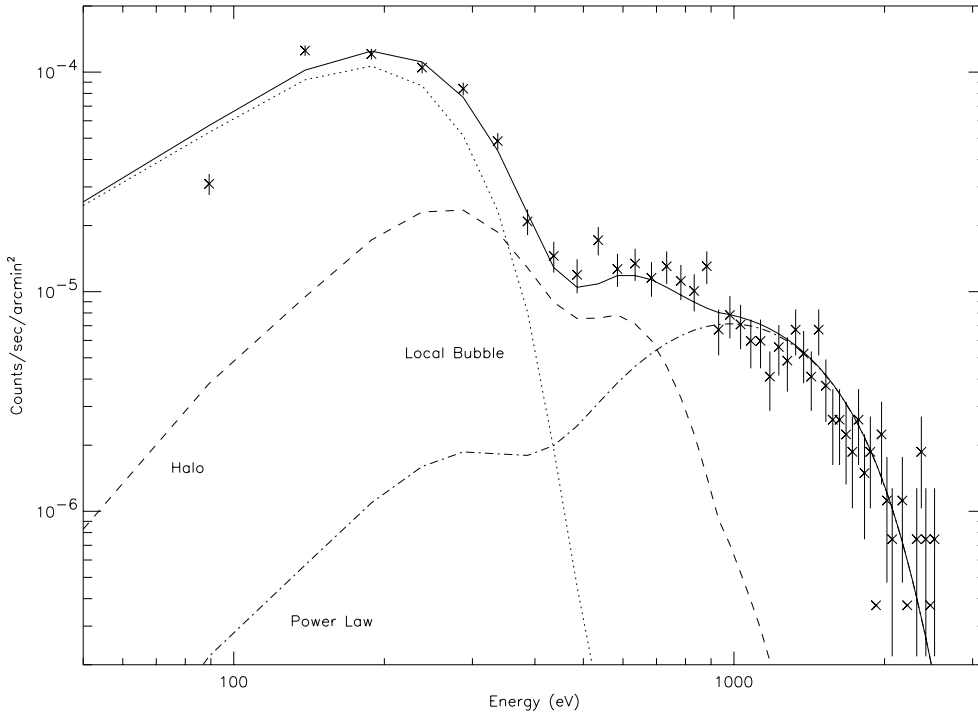


Fig. 7. Spectral fit for a typical SXR direction. The overall fit is shown together with contributions of the individual components.

The setting of a rather strict threshold on TEVS has improved the spectral fit for the deep observation (see last entry in Table 1) and although the fit is still far from acceptable, the degree of discrepancy is no worse than for some of the other poorly fitted regions in Table 1. Having already explored the halo and foreground components in some detail, it is now reasonable to concentrate on the extragalactic component; it is conceivable that these discrepancies are due to fluctuations in the power law component which are neglected by the simple extrapolation from 5 keV down to 2 keV. To test this tentative hypothesis two more free parameters are introduced into the model, namely the spectral slope and the spectral coefficient. A five parameter fit is thus performed for the deep observation rp900029 and the ranges of the parameters are tabulated in Table 2. The results are summarised in Table 3.

However, an equally acceptable χ^2_ν fit can be obtained by a wider variation in the spectral slope and coefficient than is represented by the differences between the fixed power law and that shown in Table 3. Since both the average halo and extragalactic components are significant in the 1–2 keV energy range, there is no way of separating the two effects in our measurements, especially in view of our limited knowledge about the origin and spectral properties of the extragalactic component. The best estimate one can make is to extrapolate the higher energy power law - our standard model - to the 1–2 keV range, but all our statements about the average halo component are subject to the uncertainty arising from this assumption.

Recent work by Miyaji et al. (1998) supports our results, although they have performed simultaneous spectral fits to this region using both ROSAT PSPC and ASCA data. Their model incorporates a broken power-law for the extragalactic component which steepens at $E < 1$ keV.

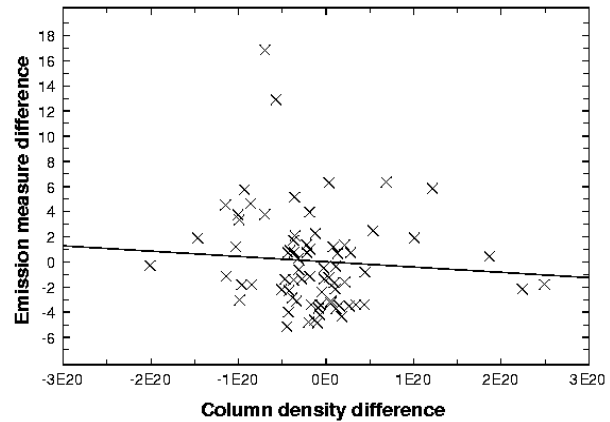


Fig. 8. Scatter plot of the deviation from the mean of each fitted halo EM (in units of $0.0032 \text{ cm}^{-6} \text{ pc}$) and the HI column density difference between the Stark and Leiden/Dwingeloo surveys. The solid line represents the expected halo EM variation as a result of this column density difference.

5. Conclusions

Our simple model continues to provide meaningful spectral fits over a large area of the sky, signifying the basic validity of the assumptions about the geometry. Residual instrument calibration uncertainties, particle contamination and scattered solar X-ray background are likely to be the principal sources of error. The discrepancies may also be attributable to long term enhancements which tend to have softer component than the cosmic ray background. Comparison of the best fit halo emission measures found as a function of position lend no positive support to the hypothesis that there is a significant hot gas distribution centred on the LG. A patchy Galactic halo hot gas at temperature $\log T$

Table 2. Parameter search space for the 5 parameter fit to the rp900029 deep observation in the Lockman field. The range of variation for each variable parameter is shown with the number of increments over the indicated range being enclosed in brackets. Fixed parameters are printed in boldface

Slab description	Spectral coefficient ph/(cm ² s keV sr)	Spectral Slope	N_{HI} 10 ¹⁸ cm ⁻²	$\log T$	Emission measure $\times 0.0032$ (cm ⁻⁶ pc)
1) Extragalactic PL	0.002–0.022(21)	0.4–2.4(21)	0.0	–	–
2) Galactic halo	–	–	0.0	5.8–6.3 (6)	2.0–5.0 (31)
3) Disk	–	–	50	–	–
4) Foreground	–	–	6.6	5.9	0.5–2.5 (11)

Table 3. Best fit results ($\chi^2_{\nu} \leq 1.6$) for rp900029 deep observation in the Lockman field

Slab description	Spectral coefficient ph/(cm ² s keV sr)	Spectral Slope	N_{HI} 10 ¹⁸ cm ⁻²	$\log T$	Emission measure $\times 0.0032$ (cm ⁻⁶ pc)
1) Extragalactic PL	0.0035±0.0005	0.7±0.3	0.0	–	–
2) Galactic halo	–	–	0.0	6.3	2.6±0.2
3) Disk	–	–	50	–	–
4) Foreground	–	–	6.6	5.9	0.90±0.10

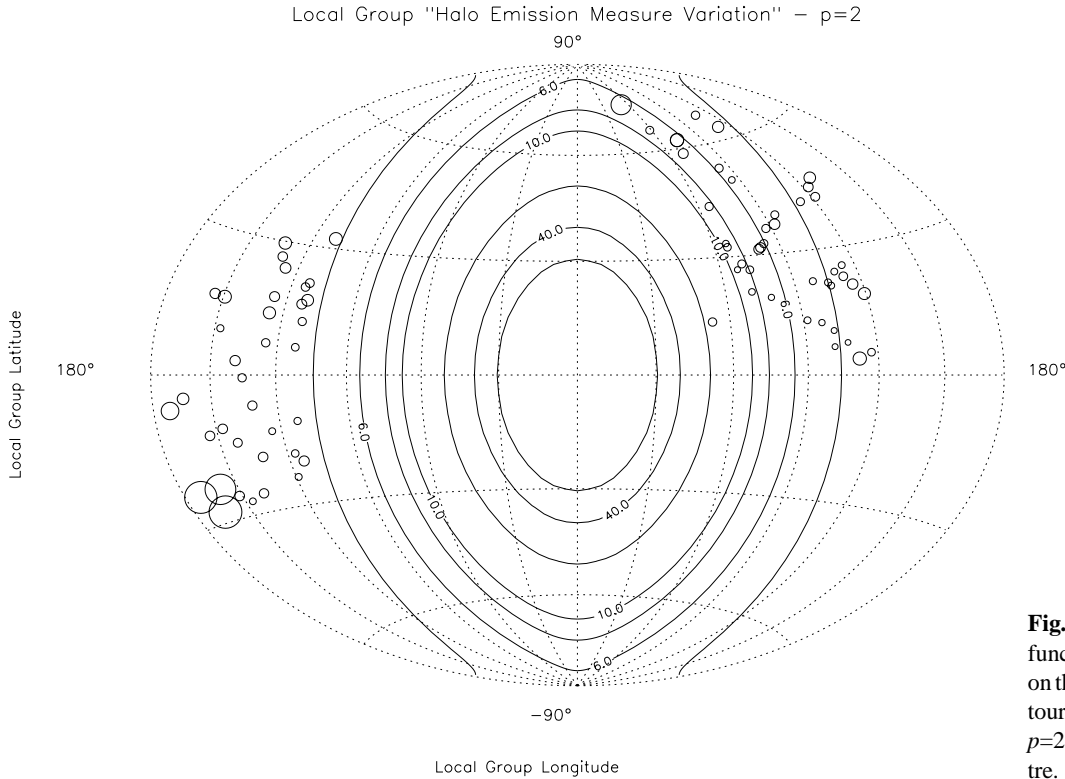


Fig. 9. LG halo EM variation as a function of LG coordinates (centred on the Andromeda nebula). The contours denote the expected EM for a $p=2$ density decrease from the centre.

= 6.3 and with an average EM of $0.02 \text{ cm}^{-6} \text{ pc}$ is much more likely.

The electron density we would attribute to any LG halo is too small to affect planned investigations of the Cosmic Microwave Background (CMB) anisotropy. It is worth noting that this electron density is only 1/10th of that of the local galactic halo. The observed fluctuations in the $\sim 10^6 \text{ K}$ halo render it

impossible to investigate the 1 keV SXRb spatial variability to better than 10% accuracy and likewise the 2 keV SXRb to better than 1%.

The spectral fitting in the Lockman hole region in comparison with the all-sky average suggests fluctuations in the power law representation of the intrinsic SXRb by approximately 50%, although we cannot be certain of separating local and true ex-

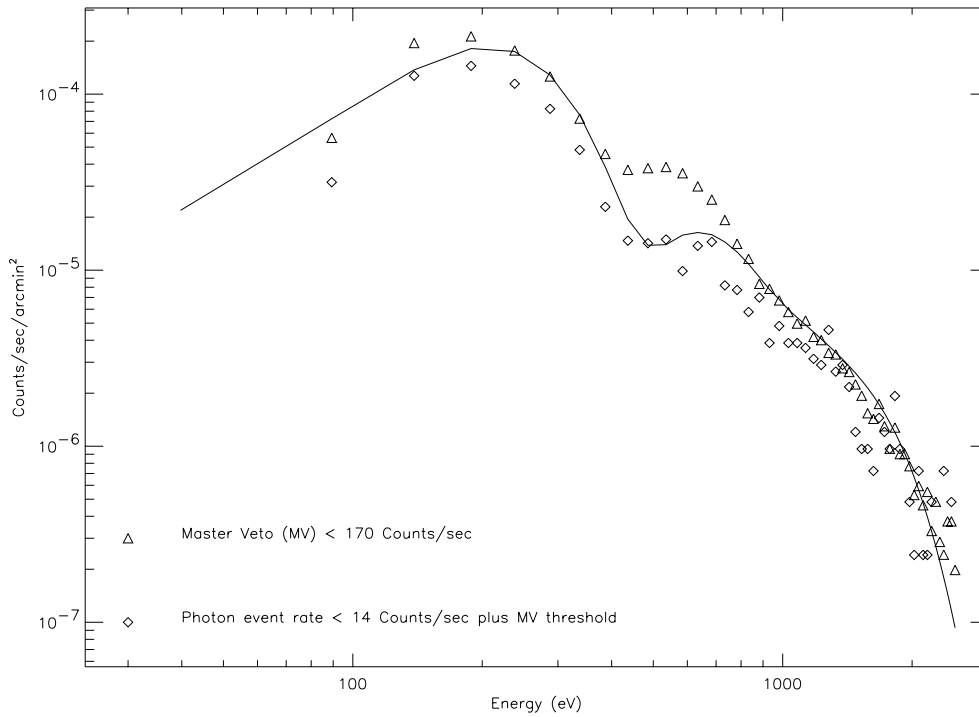


Fig. 10. Spectral plot for the deep observation rp900029 in the Lockman field. The triangles represent the spectrum generated with just the master veto threshold of 170 cts s^{-1} , while the diamonds represent the spectrum with the additional constraint of the photon event rate being below 14 cts s^{-1} . The best three component spectral fit for this region is shown by the solid line.

tragalactic sources of spatial variability. We wish to stress the difficulty in the 1–2 keV energy regime of effecting this separation.

Halo EM fluctuations are established at the 30% level over an angular scale of 5° (Table 1). Since there is likely to be less fluctuation power at smaller angular separations, claims that certain clusters of galaxies exhibit EUV excess (e.g. Lieu et al. 1996) are probably safe from this source of contamination as the spatial scales involved are smaller.

Acknowledgements. This work was partly funded by SERC, via ROSAT. The data analysis was carried out on the Imperial College STARLINK node, which is supported by PPARC. We are grateful to B.C. Monsignori Fossi for copies of his emission codes. This research has made use of data obtained from the UK ROSAT Data Archive Centre at the Department of Physics and Astronomy, Leicester University, UK. We thank the anonymous referee for constructive comments.

References

- Bloemen J.B.G.M., 1987, *ApJ* 322, 694
 Bloemen H., Duric N., Irwin J., 1993, *Proc. 23rd ICRC*, Calgary, 2, 279
 Breitschwerdt D., McKenzie J.F., Voelk H.J., 1993, *A&A* 269, 54
 Cruddace R., Paresce F., Bowyer S., Lampton M., 1974, *ApJ* 187, 497
 Hartmann D., Burton W.B., 1997, *Atlas of Galactic Neutral Hydrogen*. Cambridge University Press
 Juda M., Bloch J.J., Edwards B.C., et al., 1991, *ApJ* 367, 182
 Kahn F.D., 1994, *Ap&SS* 216, 325
 Landini M., Monsignori Fossi B.C., 1990, *A&A* 82, 229
 Lieu R., Quenby J.J., Sidher S.D., et al., 1992, *ApJ* 397, 158
 Lieu R., Mittaz J.P.D., Bowyer S., et al. 1996, *Sci* 274, 1335
 Lockman F.J., Jahoda K., McCammon D., 1986, *A&A* 302, 432
 Miyaji T., Ishisaki Y., Ogasaka Y., et al., 1998, *A&A* 334, L13
 Morrison R., McCammon D., 1983, *ApJ* 270, 119
 Pietz J., Kerp J., Kalberla P.M.W., et al., 1998, *A&A* 332, 55
 Pildis R.A., McGaugh S.S., 1996, *ApJ* 145, 811
 Plucinsky P.P., Snowden S.L., Briel U.G., et al., 1993, *ApJ* 418, 519
 Reynolds R.J., 1991, In: Bloemen H. (ed.) *The Interstellar Disk-Halo Connection in Galaxies*. Kluwer, Dordrecht, 67
 Shapiro P.R., Field G.B., 1976, *ApJ* 205, 762
 Sidher S.D., Quenby J.J., Sumner T.J., et al., 1996, *A&A* 305, 308
 Snowden S.L., Egger R., Finkbeiner D.P., et al., 1998, *ApJ* 493, 715
 Stark A.A., Gammie C.F., Wilson R.W., et al., 1992, *ApJS* 79, 77
 Suto Y., Makishima K., Ishisaki Y., et al., 1996, *ApJ* 461, L33
 White S.D.M., Navarro J.F., Evrard A.E., et al., 1993, *Nat* 366, 429